

Tuning of Static and Dynamic Mechanical Response of Laser Powder Bed Fused AlSi10Mg Lattice Structures through Heat Treatments

Jacopo Fiocchi,* Chiara Bregoli, Giulio Gerosa, Ausonio Tuissi, and Carlo Alberto Biffi

The use of additive manufacturing allows the production of complex designs, including metallic lattice structures, which combine lightness and good mechanical properties. Herein, the production of AlSi10Mg lattice structures by laser powder bed fusion is explored and consistent processing parameters are selected. Thereafter, it is demonstrated that heat treatments, specifically designed on the basis of the alloy's metallurgy, can be used to selectively induce different microstructural modifications and, consequently, finely tune the static and dynamic mechanical behavior of the aluminum lattice structures. In particular, removal of residual stresses results to be the dominant factor in allowing a smooth quasistatic compressive behavior and improving the structure's ability to absorb energy during collapse. On the contrary, the increase in ductility connected to the spheroidization of the Si network is shown to be of paramount importance in improving the structure's dynamic damping ability by allowing local plasticization.

structures exhibit numerous interesting characteristics, including low weight, high specific strength, and tunable rigidity, which suggest that their development and fielding may constitute a real leap forward for many demanding applications, such as the automotive and aerospace fields. When used as structural materials, lattice parts can also integrate two more functions, namely impact energy absorption and damping upon cyclic dynamic solicitation. The influence of different lattice geometries on the mechanical behavior of the built structures has been widely explored in literature^[2]; in particular, the effect of both different lattice designs^[3] and of density gradients^[4] on the static mechanical response of LPBFed aluminum structures has been studied. On the contrary, the effect of heat treatments on


LPBFed aluminum lattice structures has attracted lower attention, even though it has been addressed by some researchers before.^[5] Delroisse et al.^[6] noted that inclined lattice struts presented inhomogeneous microstructures in their upward and downward areas and demonstrated that a T6 treatment (solution treatment at 525 °C for 6 h followed by ageing at 165 °C for 7 h) was instrumental in homogenizing the microstructure by spheroidizing the original Si eutectic; as a foreseeable side effect, hardness was also reduced by the heat treatment. Suzuki et al.^[7] produced body centred cubic (BCC) AlSi10Mg lattice structures and explored the effect of a stress relieving treatment (300 °C for 2 h) and a solution treatment (530 °C for 6 h) on the compressive behavior of the structures themselves. Whereas the as-built samples fractured at a strain of 7.2% without reaching a stable plateau, both heat treatments were able to strongly increase ductility and induce the formation of a plateau with repeated stress drops associated with the formation of shear bands. Similar improvements of the ductility of heat-treated lattice structures were reported in the studies by Suzuki et al. and Liu et al.^[7,8] Finally, in Sugiyama et al.^[9] lattice structures with octahedral cells were built and subjected to solution treatment (530 °C for 6 h) and ageing (ambient temperature and 250 °C). Solution treatment allowed to improve ductility and induced the formation of a stable plateau upon compression. In contrast, successive natural ageing induced the appearance of stress drops, whereas ageing at 250 °C allowed to retain the smooth behavior of solution-treated samples. Accordingly, energy

1. Introduction

The rapid development of additive manufacturing techniques, including the well-known laser powder bed fusion (LPBF, also commonly called selective laser melting—SLM), is allowing the design and production of increasingly complex metallic parts, which may integrate different functionalities in a single device. In particular, additive manufacturing technologies have opened a wide space for effectively designing and fielding lattice or trabecular structures, which are regularly designed cellular materials, belonging to the broad family of porous metals.^[1] Such

J. Fiocchi, C. Bregoli, G. Gerosa, A. Tuissi, C. A. Biffi
National Research Council
Institute of Condensed Matter Chemistry and Technologies for Energy
Via Previati 1/E, 23900 Lecco, Italy
E-mail: jacopo.fiocchi@icmate.cnr.it

G. Gerosa
Politecnico di Milano
Lecco campus, Via Previati 1/C, 23900 Lecco, Italy

 The ORCID identification number(s) for the author(s) of this article can be found under <https://doi.org/10.1002/adem.202100418>.

© 2021 The Authors. Advanced Engineering Materials published by Wiley-VCH GmbH. This is an open access article under the terms of the Creative Commons Attribution-NonCommercial License, which permits use, distribution and reproduction in any medium, provided the original work is properly cited and is not used for commercial purposes.

DOI: 10.1002/adem.202100418

absorption efficiency was maximal in solution-treated samples but overageing was deemed necessary for obtaining stable properties in time. These data were then applied in the design of an impact energy absorbing system for a space lander in Kitazono et al.^[10]

Considering these available literature data, it is evident that, although the lattice geometry is the main factor in determining its mechanical response, heat treatments play a fundamental role in tuning the functional performances of LPBFed aluminum lattice structures. To expand the available knowledge in this field, this work aims at studying the effect of different heat treatments, including direct ageing, stress relieving, and low temperature annealing, on the mechanical behavior of the LPBFed lattice structures. Trabecular parts with tetragonal (or cubic diamond) unit cells were considered, as this geometry displays a good strength–density combination. Moreover, as their failure mode has been reported to be based on the formation of successive cracks at 45° with respect to loading direction,^[3] it appears of great interest to try and delay such cracking by tuning the material's properties through heat treatments. In particular, the quasi-static and dynamic compression behavior were addressed to explore the possibility of using such structures for dissipating energy during both compression to failure and loading–unloading cycles. The correlation between microstructural evolution and mechanical response was discussed, indicating that low temperature annealing may represent a promising compromise among different requirements.

2. Experimental Section

An LPBF system (mod. AM400 from Renishaw), equipped with a pulsed wave laser was used to produce AlSi10Mg lattice structures, featuring a tetragonal diamond-like structure, as shown in **Figure 1** (strut diameter and length of 1 and 2.5 mm, respectively). Unit cells and deriving samples were designed by means of structure module in Magics software by Materialize. Samples were built along the building direction (Z axis) according to the so-called lattice strategy, which is based on successive concentric scans of the laser beam (Figure 1c). To obtain sound parts,

Table 1. Process parameters used for the printing of lattice samples.

Varied parameters	Power [W]	200-225-250-275
	Exposure time [μs]	20-25-30-33-35-38-40
Fixed parameters	Scanning strategy	Lattice
	Hatch distance [μm]	90
	Point distance [μm]	90
	Laser spot size [μm]	65
	Atmosphere	Ar
	Thickness layer [μm]	30
	Platform temperature [°C]	30

processing parameters were systematically varied, as shown in **Table 1**, and the outcome was evaluated in terms of relative density. Porosity, and thereafter relative density, of the fabricated samples was measured by analyzing optical micrographs of the considered samples: micrographs of finely polished XY sections were taken (Leitz Aristomet microscope, 50× magnification) and thereafter binarized by means of ImageJ software. The ratio between pore area (black area) and dense area (white area) was assumed to correspond to the relative porosity of the sample. In the optimized condition, X-ray computed tomography (CT) was carried out on a prismatic portion of a sample, using an XTH225–ST system (Nikon, Leuven, Belgium), having an X-ray gun of 225 kV and a 16-bit flat-panel Varex 4343CT as a detector, to highlight the defects within the entire volume of the sample. The following settings were used for the measurements: 1) voltage of 160 kV; 2) 6 μm as the resolution of the detector; and 3) 105 min as scanning time.

Samples produced with optimized parameters were thereafter subjected to different heat treatments, first developed by the authors in Fiocchiet al.^[11] and further optimized in Colombo et al.^[12] Four different conditions were tested: 1) As built; 2) HT170: annealed at 170 °C for 90 min and then naturally cooled. It is a T5 ageing treatment, aimed at precipitation hardening; 3) HT263: annealed at 263 °C for 180 min and then naturally cooled. It is a stress relieve treatment, aimed at removing residual stresses without further modifying the microstructure; 4) HT294:

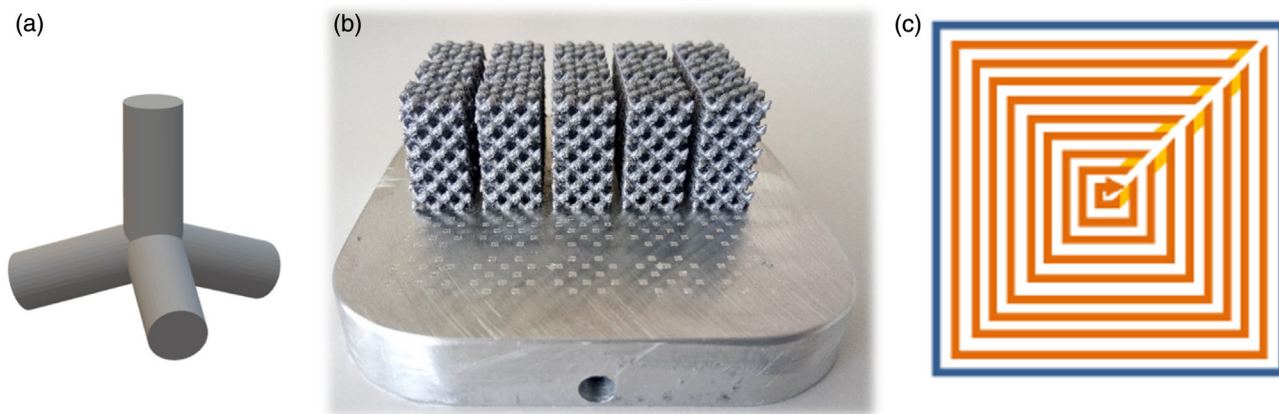


Figure 1. a) Tetragonal (or cubic diamond) unit cell; b) picture of the lattice structures produced by LPBF; and c) schematic depicting the laser path according to lattice strategy.

annealed at 294 °C for 45 min and then naturally cooled. It is an homogenization treatment, aimed at obtaining the spheroidization of the silicon network, typical of LPBFed Al–Si alloys.

Morphological analysis was carried out using scanning electron microscope (SEM Leo 430 by Zeiss) on the XY sections of samples etched in Keller’s reagent. Quasistatic mechanical properties were evaluated by compression testing with an MTS 2/M machine (strain rate of 0.015 min⁻¹), equipped with an extensometer, according to ASTM E9 standard. As widely accepted in th academic community, engineering stress and strain were computed considering the nominal section and length of the whole trabecular structure, as if it were a dense part.^[13] The damping ability of the produced parts was evaluated by dynamic mechanical analysis (DMA). A linearly actuated Instron Electropulse E3000 testing system, working in stress control mode, was used to apply a sinusoidal stress σ and record the outcoming deformation ε . Tests were carried out dynamically with a stress amplitude of 2.5 MPa. This was done by varying the applied stress between 0.1 MPa (preload) 5.1 MPa at increasing frequencies of 1, 10, 50, and 100 Hz. The $\tan \delta$ value for each testing condition was measured on the basis of the phase lag between the applied stress and recorded strain sinusoidal curves.

Finite element (FE) analyses were carried out on ANSYS mechanical 2021 for a deeper interpretation of the DMA tests’ results. In particular, as built sample and HT294 sample were addressed to highlight their different mechanical behaviors. In FE simulations, a uniform pressure was applied on each upper surface of interrupted struts (Figure 2a), so as to produce a load equivalent to the 5 MPa load applied as maximum stress during DMA tests; fixed boundary condition was set for the opposite side of the lattice structure (Figure 2a). The model was meshed with 59 349 quadratic elements (Figure 2b).

An elastoplastic isotropic mechanical behavior of the materials was considered by means of a bilinear isotropic hardening

Table 2. Parameters used to model the elastoplastic behavior of samples in FE simulations.

Material	Young modulus [GPa]	Yield strength [MPa]	Tangent modulus [MPa]	Ultimate tensile strength [MPa]
As-built	70	272.0	4147	408.2
HT170	70	308.5	2903	442.3
HT263	70	232.2	3120	343.9
HT294	70	206.7	2062	314.8

model: such a model considers a perfectly elastic behavior up to yielding point, defined by elastic modulus and yield strength, and describes plastic deformation as a linear section by a tangent modulus between yield strength and ultimate tensile strength defined. **Table 2** shows the values inserted in the FE model, which were computed on the basis of bulk mechanical properties reported in a previous study.^[14] It shall be noted that, although the Young modulus values could be theoretically considered to be slightly dependent on the heat treatment condition,^[15] such variation is generally very small in both conventionally produced and LPBFed aluminum alloys and can be therefore safely neglected.^[16,17]

3. Results and Discussion

3.1. Optimization of Processing Parameters

The energy provided by the laser to the powder bed during LPBF processing may be described by volumetric energy density (Ψ), whose expression for a PW laser is reported in Equation 1

$$\Psi = \frac{P \cdot t_{exp}}{d_p \cdot d_h \cdot s} \quad (1)$$

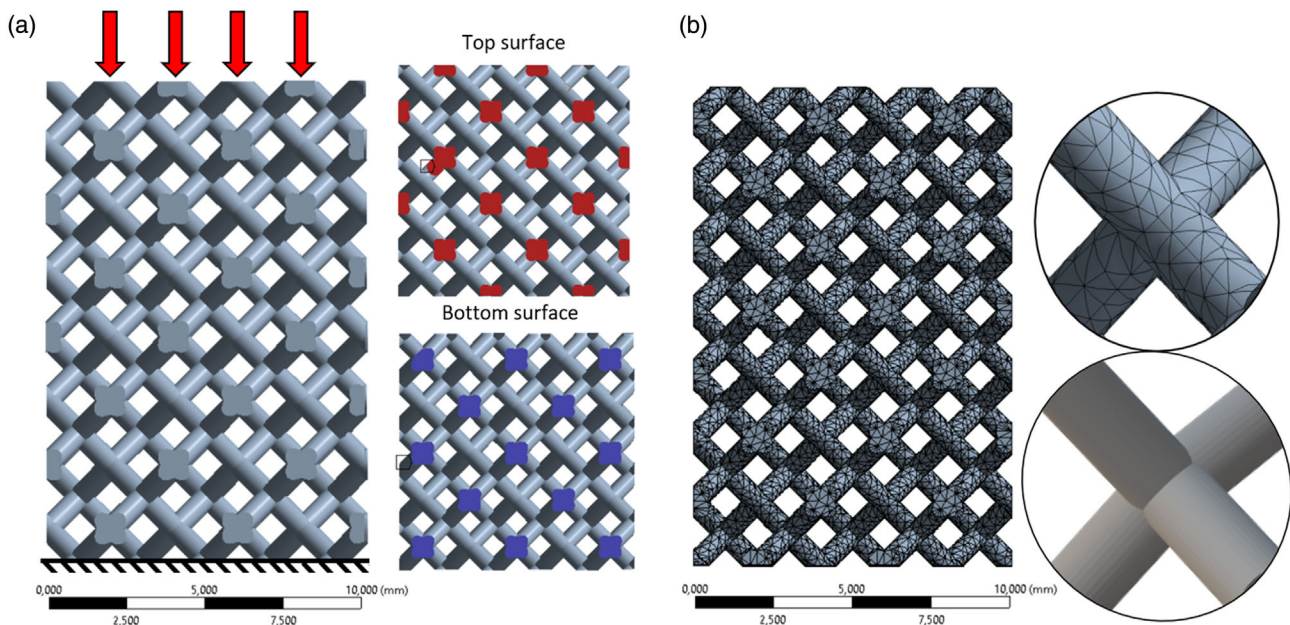


Figure 2. Model of the samples treated by FE analysis, depicting loaded areas in red, a) constrained areas in blue and b) used mesh.

where P represents the laser power, t_{exp} the exposure time, d_p the point distance, d_h the hatch spacing, and s the layer thickness.

An appropriate feasibility window was identified by varying the main process parameters (power and exposure time), which are representative of the PW emission mode, to maximize the relative density of the lattice structures. **Figure 3** shows the evolution of the relative density of the lattice samples as function of the applied Ψ . The typical trend of the relative density for LPBFed parts can be observed: a rapid increase in the relative density up to its maximum value (98% at 35 J mm^{-3}) can be observed, then the density decays smoothly for higher Ψ values. Specimens produced with different energy densities exhibit different shapes, sizes, and distribution of defects, as the prevalent defect formation mechanism varies according to energy density.^[18,19] **Figure 3b–d** shows the cross sections of lattice specimens, produced in three representative processing conditions, which can be identified from the graph in **Figure 3a**. These conditions are associated to insufficient (i.e., 13 J mm^{-3}), optimal (i.e., 34 J mm^{-3}), and exceeding (i.e., 45 J mm^{-3}) energy density. These defects can be associated to different regions of a processability map. Literature reports that different types of defects are caused by a combination of different phenomena, such as key-hole, shrinkage, balling, and lack of fusion.^[20,21] The most common defects, which can be found in LPBFed parts, are irregular porosities, due to lack of fusion (**Figure 3b**), and spherical pores, due to gas entrapment (**Figure 3d**).

The internal defects of the lattice structure produced with 34 J mm^{-3} energy density were analyzed by means of a CT scan.

A representative cross section of the lattice structure, observed along the XY plane, is shown in **Figure 4a**; the color band on the left of the picture indicates the defects' size. The porosity had no preferential distribution within the nodes of the lattice structure. On the contrary, the lattice border displays the presence of several partially melted powder particles, which increase the irregularity of the surface morphology (**Figure 4b**). This feature may be ascribed to the scanning strategy adopted during the LPBF process. The used scanning strategy implies an ellipsoidal path of the laser beam from the center to the border of the lattice element: the best degree of homogeneity on the overlapping of adjacent liquid pools could be reached, as also reported in other works.^[22] In this respect, it shall be noted that the chosen processing parameters may have a strong impact on both macroscopic features, such as geometrical accuracy,^[23] as well as on microstructural aspects, including residual stresses distribution^[24] and incipient precipitation.^[25] Nevertheless, the reduction of the amount of inner defects represents the first and main aim of this process optimization campaign, in the view of obtaining trabecular structures with satisfactory mechanical integrity. The analysis of optimized samples showed that the defect size ranged between 15 and $250 \mu\text{m}$, except few larger defects (**Figure 5a**), and the most frequent defect size lied below $100 \mu\text{m}$. Moreover, the sphericity of most of the defects was found to lie in the 0.40–0.80 range with an almost Gaussian distribution (**Figure 5b**). Two categories of defects can be observed: 1) the ones having a sphericity in the range of 0.40–0.65 and size in the range of $100\text{--}300 \mu\text{m}$, which are due to insufficient energy

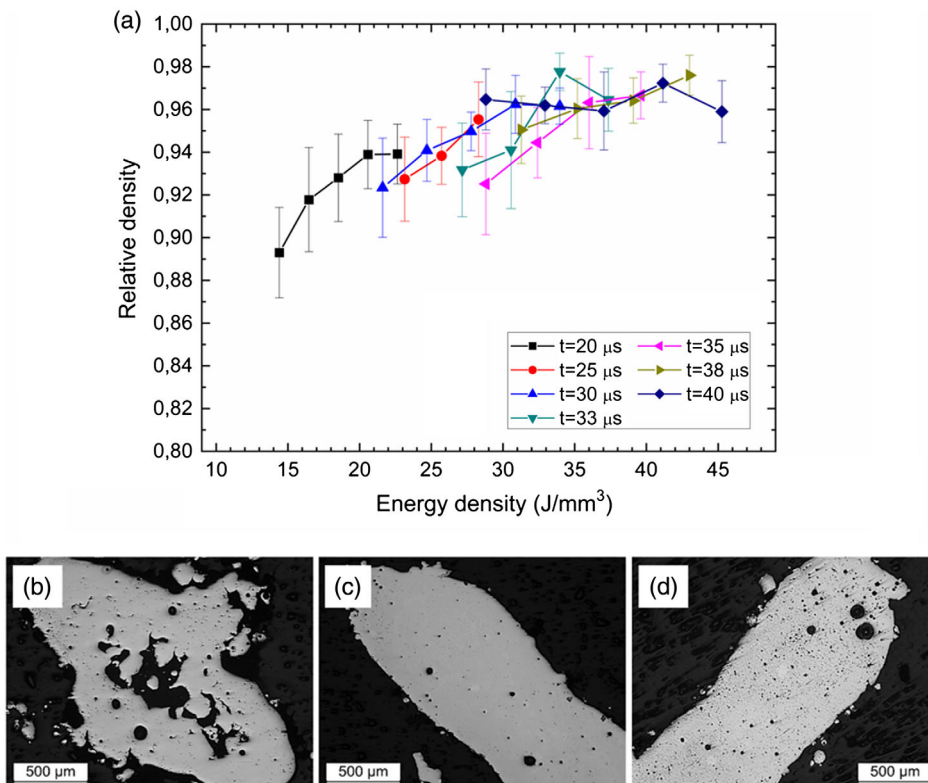


Figure 3. a) Evolution of relative density as function of applied laser energy density; representative sections of samples built with insufficient, optimal and exceeding energy density: b) 13 J mm^{-3} , c) 34 J mm^{-3} , and d) 45 J mm^{-3} .

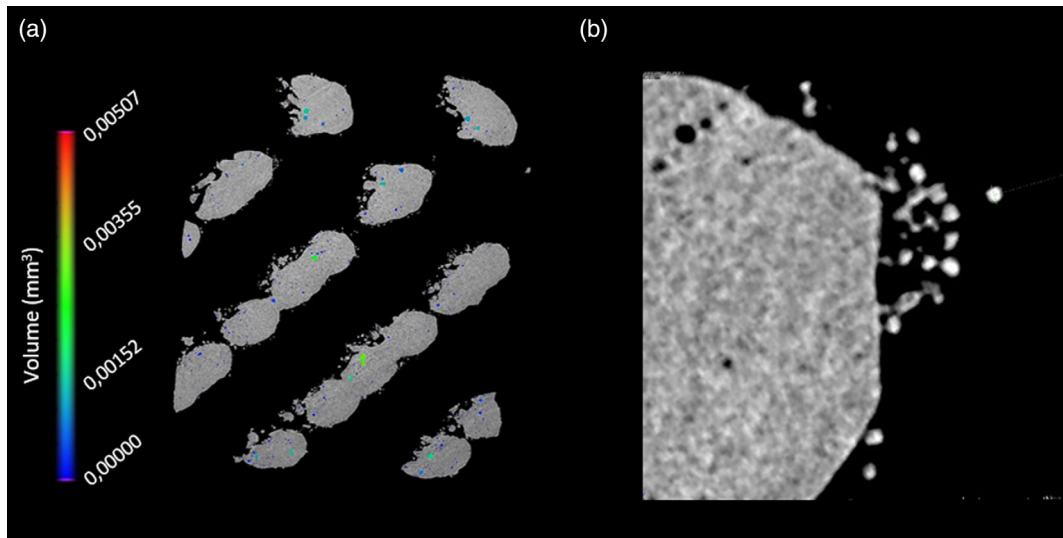


Figure 4. CT analysis of the LPBFed AlSi10Mg lattice structure: a) cross section in the XY view and b) its magnification.

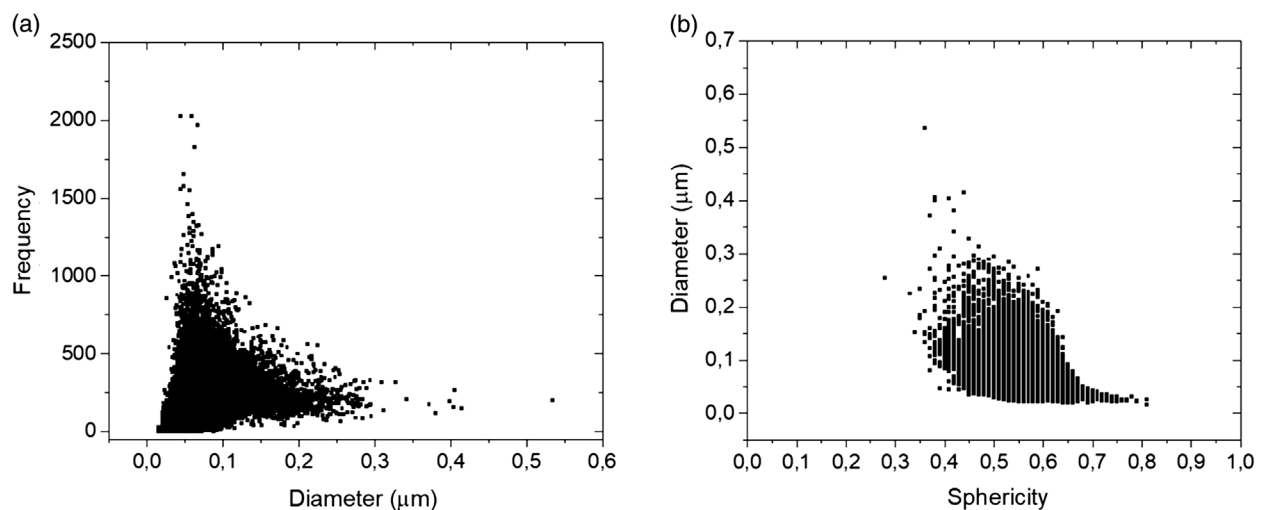


Figure 5. a) Frequency–diameter, b) diameter–sphericity trends of the defects detected by CT analysis of an LPBFed AlSi10Mg lattice structure produced with optimal parameters.

for complete melting; 2) the ones having a sphericity in the range of 0.65–0.80 and size in the range of 30–100 μm , which are caused by gas entrapment, in turn induced by the excessive energy for melting and partial vaporization. This behavior suggests that the energy irradiated by the laser beam to the powder bed was sufficient for producing high-density samples and the defects associated to incomplete melting and vaporization are both present.

3.2. Microstructural and Mechanical Characterization

The microstructure of samples produced with optimized parameters (reported in Figure S1, Supporting Information) in as-built condition shows the typical succession of melt pools, appearing as stacked semicircles in the XZ plane and as elongated stripes in

XZ plane. As already reported in previous works,^[6] the shape and orientation of melt pools are heavily influenced by the orientation of struts and also vary between nodes and struts interior areas. At higher magnification (Figure 1a), the observed microstructure shows no evident difference with the one of bulk samples and is dominated by the presence of a very fine Al-Si cellular eutectic structure. The microstructure evolution of such microstructure upon heat treatment is shown in Figure 6. It may be appreciated that the results are consistent with the ones previously reported by the authors for bulk samples^[14] and, furthermore, that no bending or warping of the lattice structures could be noted after heat treatments. The well-known cellular structure, which characterizes the as-built sample, is retained after direct ageing at 170 °C and even after the stress relieving treatment carried out at 263 °C (Figure 6b,c). On the contrary, annealing at

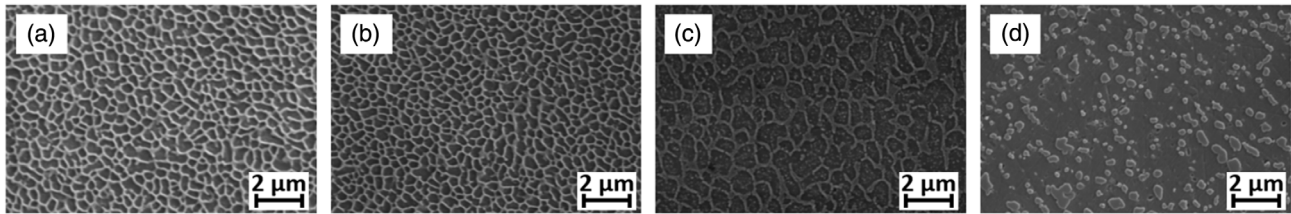


Figure 6. representative SEM micrographs of LPBFed AlSi10Mg samples in a) as-built, b) HT170, c) HT263, and d) HT294 conditions. All micrographs depict microstructures along XY plane.

294 °C (Figure 6d) induced an evident microstructural change: Si diffusion triggered the rupture of the original eutectic network and gave rise to a large amount of finely dispersed, approximately equiaxed particles, featuring dimensions of 0.5–1 μm. It shall be noted that, in addition to Si morphology evolution, other phenomena take place. In particular, ageing at 170 °C is known to activate the precipitation of Si nanoclusters^[26] and, possibly, of the Mg₂Si phase,^[27,28] thus inducing a strengthening effect. Moreover, annealing at temperatures close to 263 °C has been earlier demonstrated to be effective in removing the residual stresses, which arise from the LPBF process.^[14]

Mechanical behavior of the considered lattice structures during compression tests is shown in **Figure 7**. All curves, in every heat treatment condition, are characterized by an initial linear elastic growth up to a stress maximum, followed by a decrease in stress due to shear deformation; thereafter some low-stress oscillations take place. No plateau-like region was present in the studied conditions, as could be expected considering the selected geometry of the unit cell,^[29,30] This behavior, as evidenced by the samples photographs shown in Figure 6, is connected to the progressive bending and collapse of struts belonging to shear planes, which lie at 45° with respect to the

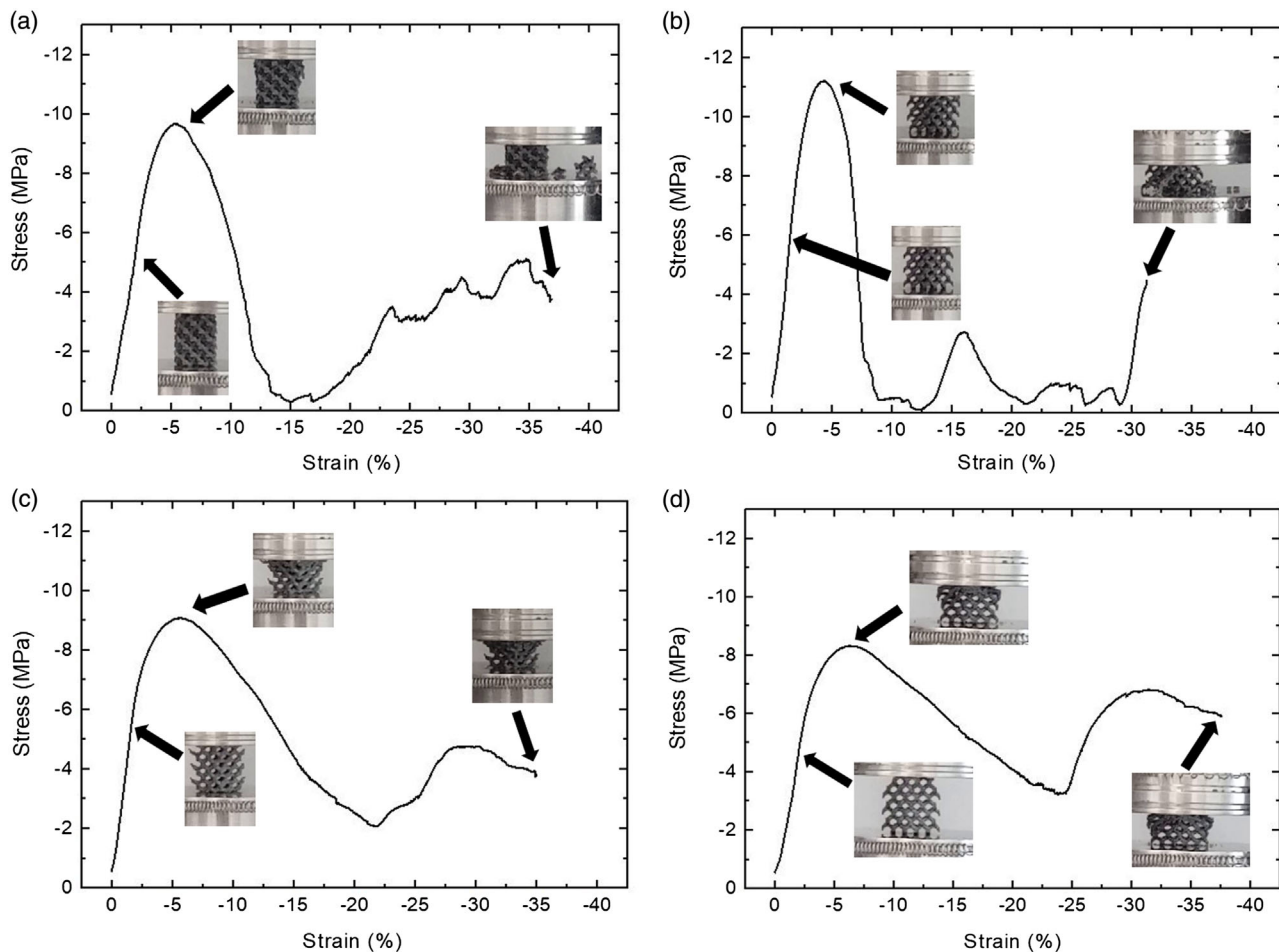


Figure 7. compressive stress–strain curves of trabecular structures in different heat treatment conditions: a) as-built, b) HT170, c) HT263, and d) HT294. Insets report video frames showing the appearance of samples in selected compressive stages.

loading direction. In particular, the first large stress peak is related to the formation of an extensive shear band encompassing the whole sample, whereas successive reduced oscillations are connected to smaller shear bands, which comprise a lower number of unit cells. Elastic moduli were found to be roughly constant for all tested samples at about 300 MPa, which represents approximately the 0.4% of the typical value of a bulk LPBFed AlSi10Mg alloy (68 GPa^[31]), in line with what reported in the study by Maskery et al.^[4] On the contrary, heat treatments had a definite influence on other mechanical parameters, including maximum stress, curve shape, and absorbed energy. It may be noted, as shown in **Figure 8**, that the maximum recorded stress, always achieved during the initial peak, was improved by direct ageing treatment (HT170), whereas it was depressed in both HT263 and HT294 samples. This trend perfectly agrees with the one of bulk parts^[14] and is strictly related to the microstructural modifications (precipitation phenomena and modification of Si morphology), as discussed in the previous paragraph. The first collapse of a shear band, corresponding to the initial stress minimum, took place at 13.2% in as-built samples, 8.7% in HT170, 21.8% in HT263, and 23.5% in HT294. Moreover, after the first stress minimum had been reached, samples treated at higher temperatures displayed a second smooth and relatively high stress hump, connected to the formation of a further shear band. In fact, visual observation of the samples during compression tests (insets in Figure 7) confirms that as-built and HT170 structures suffered the loss of numerous fragments, which were abruptly detached from the structure itself. On the contrary, HT263 and HT294 samples showed a much smoother evolution and a negligible detachment of debris. The early failure of some struts in as-built and HT170 samples may be likely justified by the presence of residual stresses, induced by the LPBF process, whose entity (about 100 and 50 MPa for as-built and HT170 parts, respectively, according to the study by Colombo et al.^[12]) may well be critical for such thin structures during compression. On the contrary, HT263 and HT294 structures may be rightfully considered devoid of any residual stress and are therefore characterized by a more regular behavior. The substantial strain extension of the first hump, together with the presence of a second smooth stress increase,

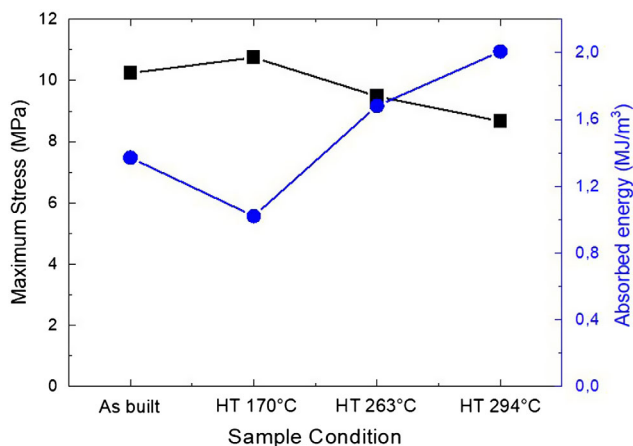


Figure 8. Maximum stresses and absorbed energies recorded during compression tests.

ensure that the structures treated at higher temperatures (HT263 and HT294) are able to absorb a higher amount of energy during compression, as shown in Figure 8. HT294 samples show a further improvement over HT244 ones, which may be appreciated in terms of higher corresponding deformation (23.5% vs 21.8%) and stress level (3.28 vs 2.07 MPa). This may be justified considering that the higher ductility of the spheroidized microstructure allowed struts to bend to a higher extent before breaking. In particular, the computed values of absorbed energy are of the same order of magnitude of the ones reported in the study by Maskery et al.^[4] for BCC AlSi10Mg lattice structures heat treated at 300 °C. In contrast, lower values were reported in the study by Kitazono et al.^[9] but the differences in unit cell and relative density shall be considered.

The damping capacity of the lattice structures in different heat treatment conditions was evaluated through dynamic compression tests: a sinusoidal loading up to 5 MPa was applied and the consequent strain was recorded as output. Such stress level was selected, as it fell in the quasielastic portion of the compression curves for all heat treatment conditions, therefore representing a realistic service condition. **Figure 9a** shows, as example, the trends of stress and strain during a cycle. The computed damping capacities ($\tan \delta$) of trabecular structures subjected to different heat treatments were computed and shown in Figure 9b as function of the applied stress frequency. As expected an evident decreasing trend of damping capacity with increasing frequency emerges.^[32] $\tan \delta$ values get close to 0 at 50 Hz and become practically negligible at 100 Hz in all treatment conditions. Moreover, it can be immediately noticed that as-built, HT170 and HT263 samples display similar behavior at all frequencies and their error bands closely overlap, even though slightly higher damping ability may be attributed to HT263 samples. On the contrary HT294 stands out, as it shows superior damping capacity for any frequency and gets grouped with the other ones at 100 Hz only. This trend appears to be in contrast with what previously reported in the study by Colombo et al.,^[31] where it was concluded that the highest damping capacity was shown by as-built samples and that the presence of residual stresses was fundamental in increasing the loss factor. On the contrary, these results suggest that the governing factor, which determines the mechanical behavior of lattice structures in dynamic loading condition, is the reduction of yielding strength of the sample and, as a consequence, the local activation of plastic deformation. This discrepancy is explained by the fact that, whereas in the study by Colombo et al.,^[31] the damping test took place in purely elastic condition, in this work, a relatively high stress was applied: it is therefore reasonable to expect that local plasticization at the nodes of the lattice structure took place, giving considerable contribution to the overall damping. In this light, lower yielding strength resistance can grant higher local plasticization and, consequently, energy dissipation.

To verify the occurrence of such plasticization, FE simulations were carried out on samples in the four heat treatment conditions. **Figure 10** compares the expected distribution of stresses in AB, HT170, HT263, and HT294 samples, when subjected to the peak load applied during cyclic tests (5 MPa).

As expected, no points characterized by stress higher than bulk ultimate tensile strength are visible, thus confirming the good agreement between experimental and numerical results.

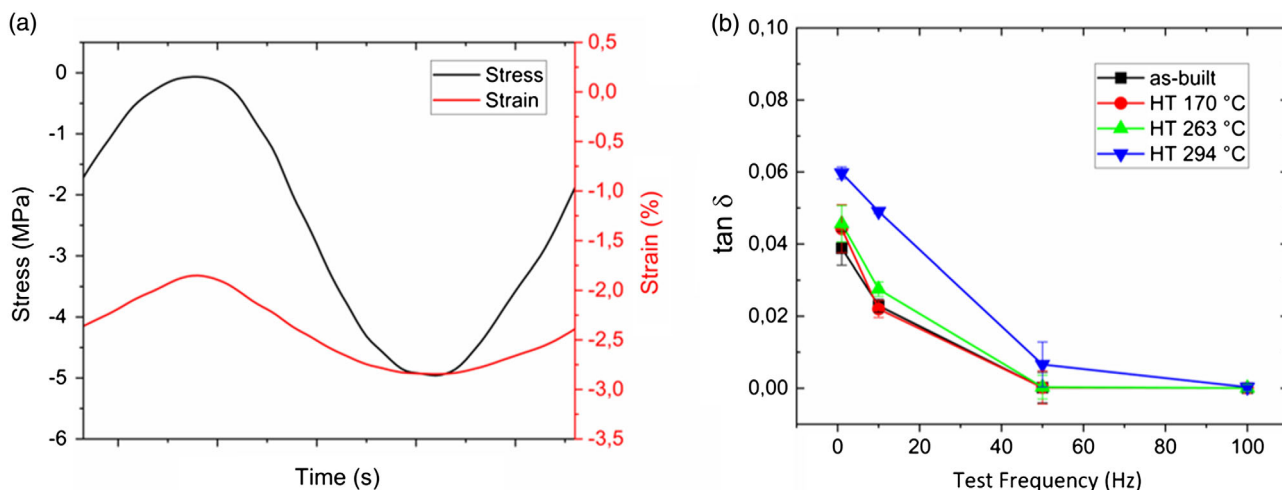


Figure 9. a) Representative loading–unloading cycle and b) damping capacity ($\tan \delta$) as function of applied test frequency of structures in different heat treatment conditions.

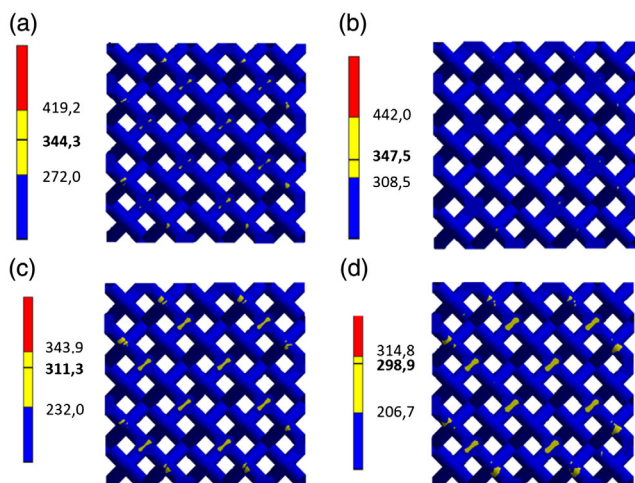


Figure 10. Distribution of equivalent Von Mises stress on the top surface for a) as-built, b) HT170, c) HT263, and d) HT294 samples during loading at 5 MPa. Bold values in the stress intensity scale indicate maximum Von Mises stress observed during FE analysis.

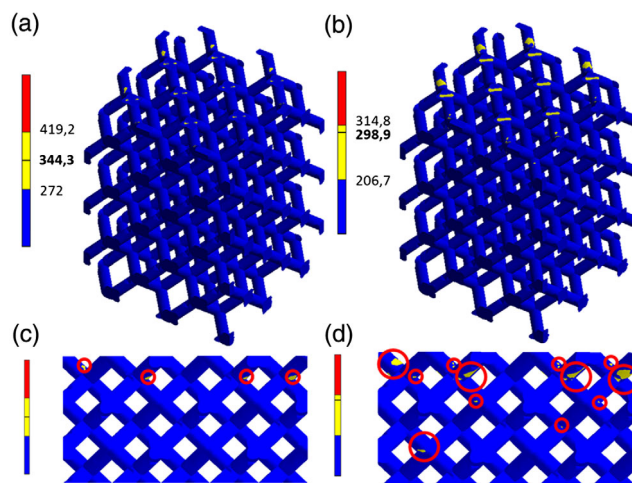


Figure 11. Distribution of equivalent Von Mises stress across a,c) as-built and b,d) HT294 samples during loading at 5 MPa. c,d) report magnifications of the upper layers of each structure. Bold values in the stress intensity scale indicate maximum Von Mises stress observed during FE analysis.

On the contrary, yellow areas, which correspond to areas where the equivalent Von Mises stress exceeds the yielding strength of each sample, are present in all samples. It should be noted that plasticization of the top surfaces of interrupted struts, i.e., of the areas that are directly subjected to loading, appear in all samples but with different intensities; such difference is further increased in other areas of the structure, as will be discussed in the next paragraph. As expected from the experimental results, HT170 samples shows the highest stress value and at the same time it presents the least local plasticization. On the contrary, HT294 shows the highest plasticization, as experimental results afore demonstrated. **Figure 11** shows a focus on the two extreme conditions, i.e., as-built and HT294 lattice structures. In particular, as reported in other available simulation results,^[33] yellow areas are more present close to the top surface of the each

samples showing that plasticization proceeds from the loaded face of the sample to the opposite side. It may be immediately appreciated that larger yellow areas are produced in HT294 samples, as shown by the red circles in **Figure 11c,d**. Such higher extension of yielded areas indicates that a more intense plasticization takes place both at the upper loaded surface and at selected points, mainly corresponding to lattice nodes, in the immediately lower layers (**Figure 11c,d**). In this respect, the extension of plasticization across different lattice layers in HT294 sample appears of particular importance, as it indicates that the whole structure takes part in dissipating the mechanical energy provided by cyclic compression, thus granting improved damping. This result further confirms that local plasticization was a decisive factor in governing the damping ability of lattice structures subjected to different heat treatments. A secondary factor, which could

explain the better damping ability of HT294 samples with respect to HT263 ones, may lie in the spheroidization of eutectic Si network, which takes place during the heat treatment at higher temperature. In fact, it has been shown that a similar microstructural evolution, albeit at a different length scale, could strongly improve damping in a cast A356 aluminum alloy through interface damping mechanism.^[34]

Received: April 8, 2021

Revised: June 19, 2021

Published online:

4. Conclusions

This article explored the processability and the possibility of tailoring the mechanical behavior of LPBFed AlSi10Mg lattice structures produced by laser powder bed fusion. Optimal process condition was selected for obtaining as high relative density as 98% of the lattice structure. It was demonstrated that static compressive behavior is mainly influenced by the removal of residual stresses: in fact, stress relieved samples (HT263 and HT294) showed a smoother behavior and a greater ability to absorb energy through plastic deformation. Conversely, the damping ability during dynamic loading–unloading cycles was shown to be dominated by the material's ductility: samples which underwent Si spheroidization treatment (HT294) stood out showing the best damping capacity, likely due to earlier plasticization of nodal regions, as confirmed by FE analysis. Moreover, the spheroidization of eutectic Si phase might increase the damping ability through interface damping mechanism. As a consequence, it may be concluded that, in the view of using aluminum lattice structures for static or dynamic energy absorption, annealing above the Si spheroidization threshold gives rise to the most desirable set of properties.

Supporting Information

Supporting Information is available from the Wiley Online Library or from the author.

Acknowledgements

The authors acknowledge Nikon for the support in the Computer Tomography analysis, Accordo Quadro CNR/Regione Lombardia n. 3866 at 17/07/2015 FHFC for financial support, Nicola Bennato and Giordano Carcano from CNR-ICMATE for their assistance in the experiments.

Conflict of Interest

The authors declare no conflict of interest.

Data Availability Statement

Research data are not shared.

Keywords

aluminum alloys, damping, laser powder bed fusion, lattice structures, mechanical properties, selective laser melting

- [1] L. Gong, S. Kyriakides, W. Y. Jang, *Int. J. Solids Struct.* **2005**, *42*, 1355.
- [2] T. Maconachie, M. Leary, B. Lozanovski, X. Zhang, M. Qian, O. Faruque, M. Brandt, *Mater. Des.* **2019**, *183*, 108137.
- [3] T. Yu, H. Hyer, Y. Sohn, Y. Bai, D. Wu, *Mater. Des.* **2019**, *182*, 108062.
- [4] I. Maskery, N. T. Aboulkhair, A. O. Aremu, C. J. Tuck, I. A. Ashcroft, R. D. Wildman, R. J. M. Hague, *Mater. Sci. Eng., A* **2016**, *670*, 264.
- [5] J. Fiocchi, A. Tuissi, C. A. Biffi, *Mater. Des.* **2021**, *204*, 109651.
- [6] P. Delroisse, P. J. Jacques, E. Maire, O. Rigo, A. Simar, *Scr. Mater.* **2017**, *141*, 32.
- [7] A. Suzuki, K. Sekizawa, M. Liu, N. Takata, M. Kobashi, *Adv. Eng. Mater.* **2019**, *21*, 1.
- [8] M. Liu, N. Takata, A. Suzuki, M. Kobashi, *Materials (Basel)* **2020**, *13*, 2487.
- [9] Y. Sugiyama, T. Miura, K. Kitazono, *Mater. Sci. Forum.* **2018**, *933*, 142.
- [10] K. Kitazono, R. Tada, Y. Sugiyama, T. Miura, *Mater. Sci. Forum* **2018**, *933*, 337.
- [11] J. Fiocchi, A. Tuissi, P. Bassani, C. A. Biffi, *J. Alloys Compd.* **2017**, *695*, 3402.
- [12] C. Colombo, C. A. Biffi, J. Fiocchi, A. Tuissi, L. M. Vergani, *Key Eng. Mater.* **2019**, *813*, 364.
- [13] M. F. Ashby, T. Evans, N. A. Fleck, J. W. Hutchinson, H. N. G. Wadley, L. J. Gibson, *Metal Foams: A Design Guide*, Elsevier, Amsterdam **2000**.
- [14] J. Fiocchi, C. A. Biffi, C. Colombo, L. M. Vergani, A. Tuissi, *J. Mater.* **2020**, *72*, 1118.
- [15] A. Villuendas, J. Jorba, A. Roca, *Metall. Mater. Trans. A. Phys. Metall. Mater. Sci.* **2014**, *45*, 3857.
- [16] W. Xianxi, Z. Weidong, L. Kunlin, W. Song, *Light Met.* **2017**, *335*.
- [17] N. T. Aboulkhair, I. Maskery, C. Tuck, I. Ashcroft, N. M. Everitt, *Mater. Sci. Eng., A* **2016**, *667*, 139.
- [18] W. R. Kim, G. B. Bang, J. H. Park, T. W. Lee, B. S. Lee, S. M. Yang, G. H. Kim, K. Lee, H. G. Kim, *J. Mater. Res. Technol.* **2020**, *9*, 12834.
- [19] J. P. Oliveira, A. D. LaLonde, J. Ma, *Mater. Des.* **2020**, *193*, 1.
- [20] B. Zhang, Y. Li, Q. Bai, *Chinese J. Mech. Eng.* **2017**, *30*, 515.
- [21] W. E. King, H. D. Barth, V. M. Castillo, G. F. Gallegos, J. W. Gibbs, D. E. Hahn, C. Kamath, A. M. Rubenchik, *J. Mater. Process. Technol.* **2014**, *214*, 2915.
- [22] C. A. Biffi, J. Fiocchi, E. Ferrario, A. Fornaci, M. Riccio, M. Romeo, A. Tuissi, *Int. J. Adv. Manuf. Technol.* **2020**, *107*, 4913.
- [23] S. L. Sing, F. E. Wiria, W. Y. Yeong, *Robot. Comput. Integr. Manuf.* **2018**, *49*, 170.
- [24] A. Salmi, E. Atzeni, *Virtual Phys. Prototyp.* **2020**, *15*, 49.
- [25] C. A. Biffi, J. Fiocchi, A. Tuissi, *J. Alloys Compd.* **2018**, *755*, 100.
- [26] J. H. Rao, Y. Zhang, K. Zhang, A. Huang, C. H. J. Davies, X. Wu, *Scr. Mater.* **2019**, *160*, 66.
- [27] R. Casati, M. Vedani, *Adv. Eng. Mater.* **2018**, *21*, 1800406.
- [28] R. Casati, M. Coduri, S. Checchia, M. Vedani, *Mater. Charact.* **2021**, *172*, 110881.
- [29] R. Wauthle, B. Vrancken, B. Beynaerts, K. Jorissen, J. Schrooten, J. P. Kruth, J. Van Humbeeck, *Addit. Manuf.* **2015**, *5*, 77.
- [30] R. Hasan, R., a., W. Mines, E. Shen, S. Tsopanos, W. Cantwell, *Key Eng. Mater.* **2011**, *462–463*, 213.
- [31] C. Colombo, C. A. Biffi, J. Fiocchi, D. Scaccabarozzi, B. Saggini, A. Tuissi, L. M. Vergani, *Theor. Appl. Fract. Mech.* **2020**, *107*, 1.
- [32] F. Rosa, S. Manzoni, R. Casati, *Mater. Des.* **2018**, *160*, 1010.
- [33] G. Scalet, C. Biffi, J. Fiocchi, A. Tuissi, F. Auricchio, *IOP Conf. Ser. Mater. Sci. Eng.* **2021**, *1038*, 012057.
- [34] V. H. Carneiro, H. Puga, J. Meireles, *Mater. Sci. Eng., A* **2018**, *729*, 1.